Article

Comparison of Pixel- and Object-Based Classification Methods of Unmanned Aerial Vehicle Data Applied to Coastal Dune Vegetation Communities: Casal Borsetti Case Study

Michaela De Giglio [1,*], Nicolas Greggio [2] , Floriano Goffo [1], Nicola Merloni [3], Marco Dubbini [4] and Maurizio Barbarella [1]

[1] Civil, Chemical, Environmental and Materials Engineering Department-DICAM, University of Bologna, Viale Risorgimento 2, 40136 Bologna, Italy; floriano.goffo@studio.unibo.it (F.G.); maurizio.barbarella@unibo.it (M.B.)

[2] Interdepartmental Centre for Environmental Science Research (CIRSA), Lab. IGRG, BiGeA Department, University of Bologna, Via S. Alberto 163, 48100 Ravenna, Italy; nicolas.greggio2@unibo.it

[3] Scientific High School A. Oriani of Ravenna, Via C. Battisti, 2, 48121 Ravenna, Italy; nicolamerloni@Isoriani.istruzioneer.it

[4] DiSCi, Geography Sec., University of Bologna, Piazza San Giovanni in Monte 2, I-40124 Bologna, Italy; marco.dubbini@unibo.it

* Correspondence: michaela.degiglio@unibo.it

check for updates

Abstract: Coastal dunes provide the hinterland with natural protection from marine dynamics. The specialized plant species that constitute dune vegetation communities are descriptive of the dune evolution status, which in turn reveals the ongoing coastal dynamics. The aims of this paper were to demonstrate the applicability of a low-cost unmanned aerial system for the classification of dune vegetation, in order to determine the level of detail achievable for the identification of vegetation communities and define the best-performing classification method for the dune environment according to pixel-based and object-based approaches. These goals were pursued by studying the north-Adriatic coastal dunes of Casal Borsetti (Ravenna, Italy). Four classification algorithms were applied to three-band orthoimages (red, green, and near-infrared). All classification maps were validated through ground truthing, and comparisons were performed for the three statistical methods, based on the k coefficient and on correctly and incorrectly classified pixel proportions of two maps. All classifications recognized the five vegetation classes considered, and high spatial resolution maps were produced (0.15 m). For both pixel-based and object-based methods, the support vector machine algorithm demonstrated a better accuracy for class recognition. The comparison revealed that an object approach is the better technique, although the required level of detail determines the final decision.

1. Introduction

Sand dunes are key environmental elements of coastal systems. They represent one of the few natural barriers that can defend the inland territories from extreme high tides, storms, and tsunamis, by absorbing the wave energy. Moreover, they have a significant role in the coastline dynamics, by balancing the erosion and/or accretion phenomena [1]. Dunes also constitute unique habitats and represent corridors that connect the diverse neighboring ecosystems [2]. However, over the last half

century, dune systems have undergone habitat loss, and the coastal dunes of Mediterranean areas are among the most vulnerable ecosystems as they are seriously threatened by urbanization and mass tourism, particularly those of the north Adriatic region [3–6]. In a detailed study by Sytnik et al. [3], they reported on the large modifications to the coastal ecosystem of the Casal Borsetti dunes (Ravenna, Italy) study area over the last century. The majority of these modifications have directly affected the local dune systems, while being aimed at the mitigation of erosion phenomena and development of beach touristic infrastructures.

Human disturbance has had effects on the structure, composition, and function of plant communities, which are sensitive indicators of the state of these environments [7,8]. In effect, coastal sand dunes shift between states of activity and stability across the seasons and years [9,10]. Some dunes remain 'stable', perhaps for many decades or centuries, whereas others are 'dynamic', and can maintain an equilibrium between cyclical mobility and stability [11]. Dunes can become active over their entire surface, in particular in areas of present or past vegetation disturbance [12]. As reported by Fabbri et al. [13] (and references therein), many factors can affect dune dynamics, including the sand supply, dune/beach exchanges, beach topography and fetch effects, vegetation species and cover, climate, marine meteorological conditions, and human impact.

Vegetated dunes are fixed and stable, while bare sand dunes are more prone to sand mobilization and erosion. Indications of dune mobility are traditionally based on climatic variables, such as rainfall, temperature, and evapotranspiration, although, except for anthropogenic factors, wind energy is the only limiting factor for the vegetation cover [14].

Beach–dune systems include the dune, its vegetation cover and coastal geomorphology, and the local dynamics (e.g., wind regime, beach typology, erosion/accumulation rate), and these continuously interact with each other. Plant communities in the dune vegetation communities select and promote their own preferred environmental conditions, which stabilizes the dunes [15]. The vegetation communities and cover reflect the conservation state of the dunes and its analysis is used to study the phases of dune evolution and to gather information about entire coastal systems [16–18].

Nowadays, data on dune topography, reflectance, and vegetation cover are usually achieved through direct field sampling [19,20], photointerpretation of aerial and satellite ortho-imagery [21], light detection and ranging (LiDAR) point cloud analysis [22,23], terrestrial laser-scanning surveys [24], and ground differential global positioning system (GPS) measurements [25]. Furthermore, hyperspectral and multispectral aerial and space-based data have been applied to detect different degrees of activity and vegetation cover density [16]. The main limitations of these last systems are their high costs for a high resolution and their insufficient availability during the periods of interest [26]. Moreover, although these images provide useful information on global and regional scales, some processes need multi-temporal observations at a local scale [27].

In recent years, sensors installed on unmanned aerial vehicles (UAVs) have offered many technical and economic advantages for coastal sand dune monitoring [24,28]. To date, most studies have been aimed at the evaluation of coastal systems, and of dunes in particular, using digital RGB (red, green, blue) cameras to build accurate digital surface models with a high spatial resolution [29]. Instead, in the present study, we investigated the use of a UAV equipped with a camera that acquired images at red, green, and near-infrared wavelengths. Pixel-based and object-based approaches [11] were tested and compared for the recognition of the vegetation communities that were growing along the coastal dune system. The advantages and disadvantages of these methods were also investigated. Therefore, the aims of this study were to (i) verify the applicability of multispectral data collected using a UAV platform for the identification/discrimination of fragmented and interspersed coastal dune vegetation communities and (ii) determine the best performing classification method between pixel-based and object-based approaches for multispectral data in the case of disturbed dune vegetation communities.

2. Materials and Methods

2.1. Study Area

The investigated dune is located near the small touristic village of Casal Borsetti (Ravenna, Italy; Figure 1a). In light of the complexity, variability, and vulnerability of the small dune belt considered, a detailed description of both the regional settings and the study area is required.

The territory surrounding the city of Ravenna has been strongly anthropized and industrialized, and in the relevant natural areas, intensive agriculture and tourist facilities coexist [30]. Since the 1960s, the establishment of tourist infrastructures directly along the coastline of this area has resulted in widespread dune damage and destruction. Where the dunes have not been completely flattened to the ground, they have undergone huge fragmentation [4,31]. The natural coastal system has been substituted with the new structures that are directly exposed to climate-change effects, such as a rise in the level of the sea, sea storms, flooding events, and marine erosion [32]. As reported by Sytnik et al. [6], the sector where the study area lies has shown the highest rates of coastal erosion of the last six decades.

Nowadays, all of the remaining dunes are included within the Po Delta Regional Park, as a Special Protection Area (Directive 2009/147/EC "Birds") and a Site of Community Importance (Directive 92/43/EEC "Habitat"). The Regional Park is also included in the UNESCO World Heritage list.

The dune investigated is 350 m long and 60 m wide. The mean dune elevation is 2.5 m above sea level (a.s.l.), and the maximum elevation is 3.5 m a.s.l. (to the north of the site). It is one of the last stretches of dunes with psammophytic vegetation, which is very important for the conservation of coastal biodiversity [33,34].
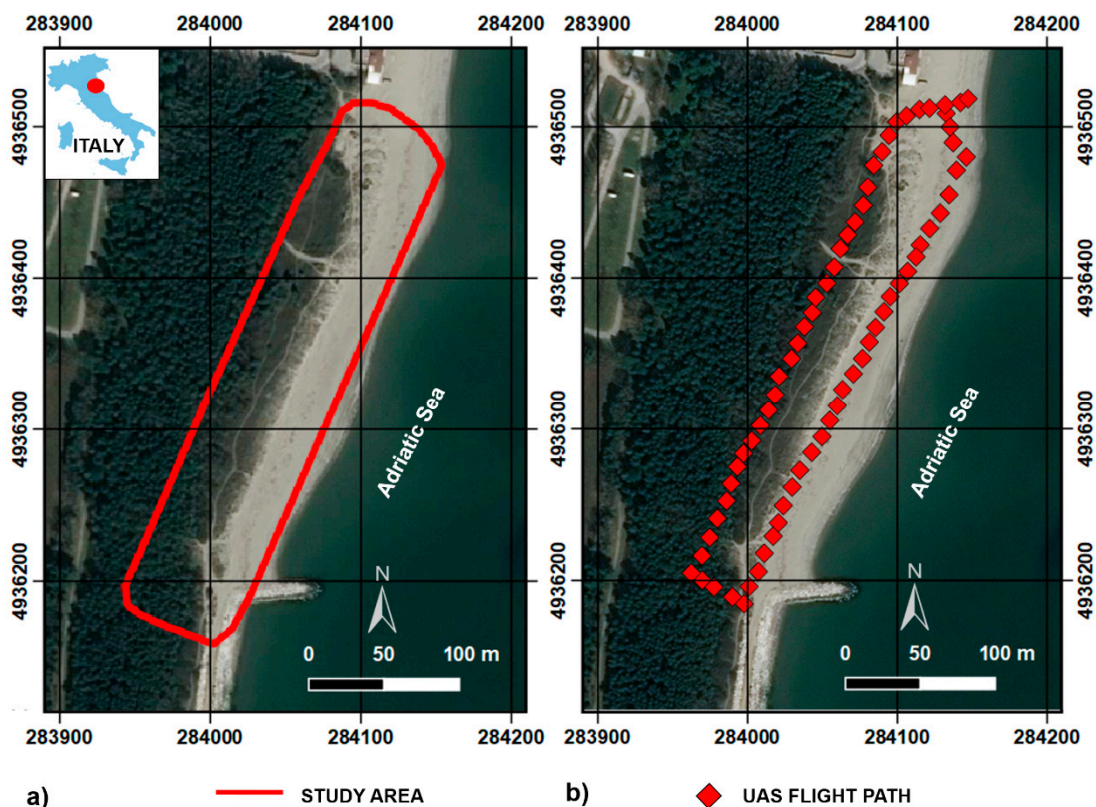
Figure 1. (**a**) Study area: Casal Borsetti dune, Ravenna, Italy. (**b**) Unmanned aerial vehicle flight path. The red squares correspond to the centers of acquisition (WGS84/ UTM zone 33N) (Image background: Google Earth).

While limiting themselves to the vegetation, many authors have described the typical zonation for the north Adriatic coastal dunes based on strips parallel to the coastline [35,36]. In agreement with the

definitions of Directive 92/43/EEC "Habitat", and in light of the recent publication of Merloni et al. [37], from the sea going inland, the zonation consists of annual pioneer species, embryo dunes, white dunes, *Malcolmietalia* grassland, grey dunes, shrubby plant communities, and coastal pine woods (Figure 2).

The annual pioneer species described as *Salsolo kali–Cakiletum maritimae* (EUNIS Code B1.12; hereafter referred to as CA) grow close to the shoreline (within a few meters), and they aid in the formation of the dunes where the organic matter brought by the sea accumulates. The main ephemeral species are *Cakile maritima*, *Salsola tragus*, and *Chamaesyce peplis* [37,38]. Moving inland, the dunes start to become semi-stable, and the embryo dune vegetation described as *Agropyretum* (*Echinophoro spinosae–Elymetum farcti*; EUNIS Code B1.3; hereafter referred to as AG) includes psammophilous perennial plants, such as *Elytrigia juncea* (=*Agropyron junceum*), *Echinophora spinosa,* and *Calystegia soldanella*, and these capture the sand as it is moved by the winds, providing the vertical growth of the dune. The white dune community is present in the inner areas where the dunes become more stable, which is also described as *Echinophoro spinosae–Ammophiletum australis* (EUNIS Code B1.3; hereafter referred to as AM). This habitat usually covers 50% to 60% of the total area, and represents a semi-permanent stage, as the roots of *Ammophila arenaria*, *Echinophora spinosa*, and *Eryngium maritimum* form dense felts that promote dune consolidation. Behind the white dunes, where salt winds, coastal erosion, and burial by sand do not affect the vegetation, there are the grey dunes (*Tortulo–Scabiosetum*; EUNIS Code B1.4; hereafter referred to as GD), which are colonized by perennial species, such as *Lomelosia argentea*, *Fumana procumbens*, and *Teucrium polium*, and which have a significant carpet of mosses and lichens (e.g., *Tortula ruraliformis*, *Cladonia convoluta*).

A complication with respect to the theoretical distribution so far described is seen here by *Malcolmietalia* grassland (EUNIS Code B1.4; hereafter referred to as MG), which arises where trampling, salty winds, and disturbance occur. This plant community is mixed with AG, AM, and GD, and it can cover large surfaces [35]. The main diagnostic species are the annual plants *Silene canescens* and *Vulpia membranacea*, which are typically found alongside allochthonous species, such as *Ambrosia coronopifolia*.

A rapid change occurs when moving further inland, where shrubby plant communities settle into depressions where they replace the grey dune vegetation (EUNIS Code B1.63; hereafter referred to as the J habitat), e.g., *Juniperus communis* and *Phillyrea angustifolia*. This narrow belt of shrub is in continuity with the coastal pine woods (EUNIS Code B1.7; hereafter referred to as the P habitat), where *Pinus pinaster* and *Pinus pinea* are the dominant species.

Along the Casal Borsetti dunes in particular, this vegetation succession is often fragmented, with each becoming interspersed with the others; this has generated an atypical vegetation mosaic. Consequently, five vegetation classes were established for the technical classification requirements here, which represent the most significant evolutionary stages of these dunes. For graphical reasons, the previously reported EUNIS Codes are henceforth substituted by the following vegetation community abbreviations: "Bare sand and *Cakiletum*" (BSCA), "*Agropyretum* and *Ammophyletum*" (AGAM), GD, MG, and "Coastal shrub and arboreal formations" (CSAF) (Figure 2).

The BSCA class represents the merging of bare sand areas and *Cakiletum*, where *Cakiletum* species are always <5% of the entire coverage, even under conditions of naturalness and in the absence of disturbance. Moreover, *Cakiletum* habitats are systematically swept during summer beach cleaning operations, which destroys all of the growing plants.

Agropyretum has a relatively high presence, even if it also partly suffers from cleaning and trampling activities. Due to these anthropic disturbances, its main species (i.e., *Agropyron junceum*) grows into the next formation, the *Ammophiletum*. These two communities have thus been merged into the "Perennial herbaceous vegetation of the embryonic and white dunes" class (i.e., AGAM). *Ammophyletum* is not abundant, even if *Ammophila arenaria* grows luxuriantly in small areas. This union is also justified from an ecological point of view, because these two represent the perennial herbaceous vegetation that is typical of both embryonal and white dunes distributed along all Mediterranean littoral areas (*Ammophiletalia australis*) [33].

The GD is the third class considered. GD is found as a homogeneous strip that is almost totally covered in mosses (*Tortulo–Scabiosetum*).

The MG vegetation species are widespread within different habitats, both for AGAM and GD, and they tend to cover even large surfaces, because of both natural and anthropogenic disturbance. Indeed, the MG settlement is mainly linked to the frequent passage of people, which creates erosion of the perennial vegetation cover.

Finally, the J and P habitats have been merged into the CSAF, which mainly includes *Pinus pinaster*, *Juniperus communis*, *Eleagnus sp.*, *Pyracantha coccinea*, *Tamarix gallica*, and *Quercus ilex*. An example of a *Populus × canadensis* tree (located in the northern area of the dunes) is also included in this class. This tree is considered to be a naturalized neophytic species that mostly grows in sandy soils that are damp for most of the year, such as riverbeds or around sandy quarries. However, it can sometimes also be found in 'back-dune' environments, although it is not typical of this kind of environment.
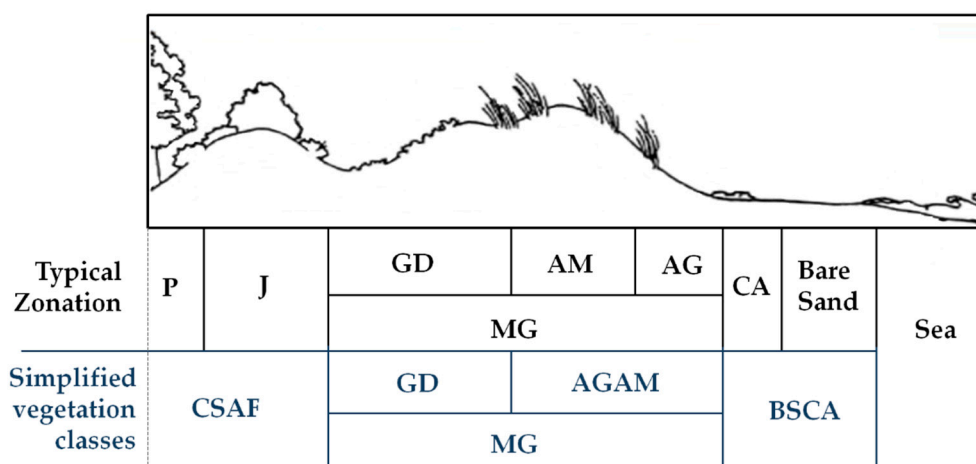
Figure 2. Schematic representation of the typical vegetation zonation [34] and the five simplified vegetation classes adopted in the present study after the in-situ botanical survey. For abbreviations, see main text.

2.2. Data Acquisition and Analysis

This analysis of the vegetation communities was based on a three-band orthoimage obtained through a photogrammetric pipeline from a dataset acquired using a UAV. The UAV platform used was an ESAFLY A2500 hexacopter (SAL Engineering, Modena, Italy). It was equipped with a commercial multispectral camera (Tetracam ADC Micro) that acquired images in the green, red, and near-infrared (NIR) bands, centered respectively at 550, 650, and 800 nm. The camera had only one sensor (Aptina CMOS; 6.55 mm × 4.92 mm; pixel size, 3.12 micron), which was screened with a filter array (Bayer RGB) in a 'checkerboard' pattern [39]. Moreover, the lens on the multispectral camera had an optical low-pass filter that stopped the blue band, but it did not have a filter to stop NIR. Through the combination of the filter in the lens with the filter array, each pixel can capture only one band between the green, red, and NIR bands, relating to its position in the checkerboard. For each pixel, it was possible to reconstruct the values of the two missing bands by interpolation of the corresponding measured values in the adjacent pixels [39]. The proprietary software PixelWrench2 (PW2) provided with the multispectral camera was used to manage this operation.

As the camera was based on the rolling-shutter acquisition system with a total frame creation time of a few milliseconds, the images were acquired with a drone translation speed of 4 m/s and with a constant flight altitude of 80 m above ground level, giving a ground sample distance of 0.03 m. These technical choices avoided blur-motion effects, thus avoiding subsequent problems in the image processing. Furthermore, the UAV had a stabilization system that consisted of a gimbal stabilized with

two brushless motors on two axes (i.e., roll, pitch), with mechanical and magnetic cardanic damping and inertial reference with high speed, which allowed for stable framing [40].

The hexacopter was equipped with a single-frequency global navigation satellite system (GNSS) receiver with a code solution. It was used for both the control and definition of the programmed flight path (with longitudinal overlapping and side slap of 80%), and for the coordinate definition of the multispectral chamber centers of acquisition (Figure 1b). These approximate camera positions were used as estimated solutions for the reconstruction of the exterior image orientation in the photogrammetric pipeline, using the approach based on the structure from motion algorithms [41]. Five ground control points (GCPs) were positioned on the ground (i.e., four targets plus the master station), to optimize and increase the accuracy of the self-calibration process for an estimation of the camera interior orientation parameters (i.e., focal length, main point, lens distortion parameters), for a definition of the parameters of the external orientation, and also to obtain more accurate georeferencing. The five targets were sufficient for the optimization process through the bundle adjustment algorithms. Indeed, as recently published by Sanz-Ablanedo et al. [42], to reach a maximum level of relative accuracy, assessed in terms of the root mean squared error/ground sample distance, 2.5 GCPs are sufficient for every 100 images. In this case, the total number of images used was <100, and of these, <30 images were aligned longitudinally and consecutively. The target coordinates were measured using a geodetic dual-frequency GNSS receiver (Topcon GB500) in rapid-static mode. The International GPS Service for Geodynamics permanent station of Medicina (Bologna, Italy) and the European Reference for Quality Assured Breast Screening and Diagnostic Services permanent station of Porto Garibaldi (Ferrara, Italy) were used to define the positions of the GCPs in the WGS84 system. The chosen projection system is UTM 33N [43].

The data obtained from the survey were raster images (ground sample distance, 0.03 m) which were composed of a single matrix of digital numbers (DN) and stored in a raw format. These files were pre-processed in PW2 to reconstruct the information for the three bands, and exported as single tri-band TIFF (Tagged Image File Format) images. The PW2 was calibrated to account for the actual exposure conditions using a RAW image of the calibration tag, acquired under the same lighting conditions as the studied images. This procedure does not convert the sensor output to reflectance [40], and therefore, the subsequent analysis was based on the DN values. The tri-band TIFF images were then processed using the photogrammetric pipeline implemented in Agisoft Photoscan Professional (Agisoft LLC, St. Petersburg, Russia). In the first step, the approximate position and orientation from the GNSS and inertial measurement unit of the drone were associated with each image. In this way, a sparse point cloud model of the scene was created. Through this model, the external orientation parameters of each individual frame were recalculated. A preliminary dense cloud model was then created. The information relating to photogrammetric GCPs was then entered, with manual collimation of each GCP identified for each individual image. The dense cloud model was linearly transformed using seven similarity transformation parameters, which only compensated for linear model misalignment. The next optimization phase then removed non-linear deformations of the model and provided accurate geo-referencing based on the known GCP coordinates [24]. Through the constraints defined by the GCPs by means of the bundle adjustment algorithm, this step allowed a recalculation of the parameters of external and internal (self-calibration) orientation. The dense cloud model was then recreated. The optimization was used to ensure correct scaling and geo-location, to improve the camera interior and exterior parameters, and to correct for any systematic error and/or block deformation. Successively, a polygon mash was generated based on the previously built dense point cloud. Finally, the digital surface model and the orthoimage were generated with a resolution of 0.15 m. The orthoimage produced maintained the three channels (i.e., green, red, NIR) that were essential for the later vegetation analysis [43].

To perform the classification, the areas of interest of five vegetation classes were defined by both direct botanical field surveys and photo-interpretation. The areas of interest surveyed in the field were measured with dual-frequency GNSS instrumentation (Leica GPS1200) using the real-time kinematic

(RTK) technique. The differential corrections were received through the ItalPoS Network service [44]. The ItalPos network provides a network-based (N)RTK system, and specifically, the real-time service is based on the master-auxiliary approach, MAX [45]. The adopted cartographic reference system for all of the data produced is WGS84-UTM33N.

Finally, to collect the ground truth control points for the map classification validation, another NRTK survey (same equipment and procedure as described above) with botanical support was conducted in-situ, with the identification of 300 points of defined vegetation classes (Figure 3). The final accuracy of the NRTK coordinates was 6 cm to 8 cm in planimetry and 8 cm to 10 cm in altimetry. These values are very acceptable considering that the size of the image cell was 15 cm × 15 cm.
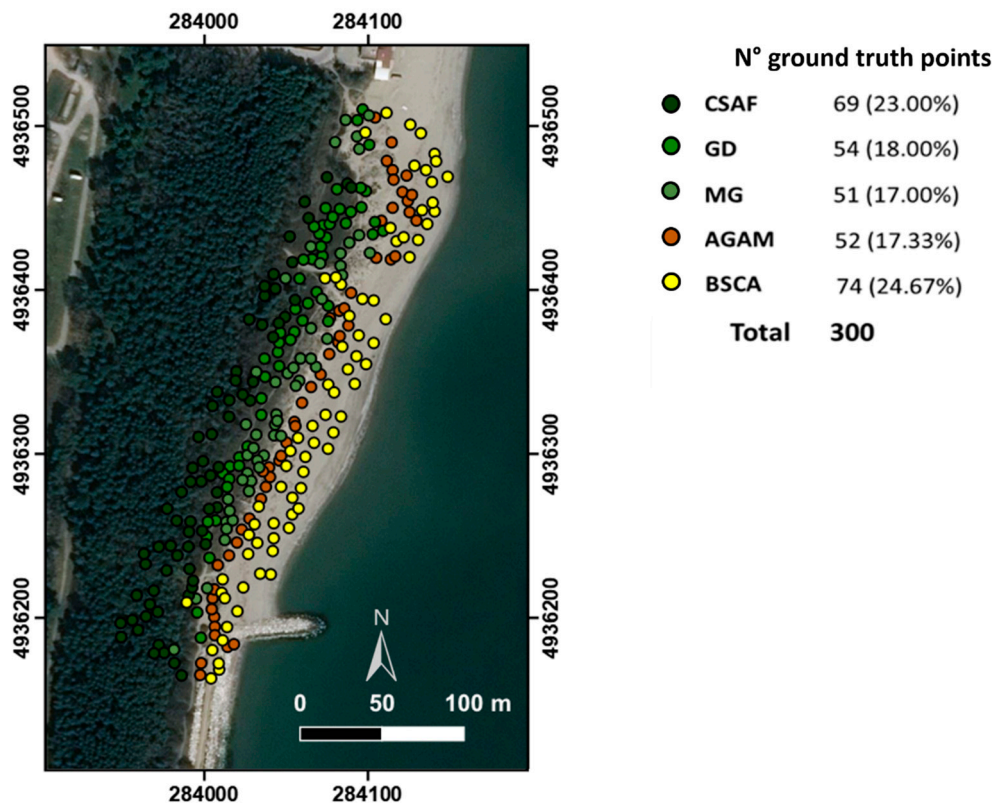
Figure 3. Map of the ground truth points used to classify the validation of results. For abbreviations, see main text.

2.3. Classification Methods

In this study, both pixel-based and object-based classification methods were applied to define the dune vegetation communities. The pixel-based classifier considers the information for the spectral signature of the individual pixels. In contrast, the object-based method classifies objects, i.e., groups of pixels with relatively homogeneous properties, that are created in a preliminary phase known as segmentation. These have intrinsic features, like information derived from the direct spectral observation and geometric properties, and contextual features that describe the relationships between multiple objects [46]. In both approaches, supervised classification algorithms were used. They both required previous knowledge of the vegetation in the study area. Beyond the complicated real field situation, the class selection was also driven by the technical feasibility of discrimination with automatic methods.

The normalized difference vegetation index was extracted from the multi-band orthoimages before the classification. The analysis started by applying the most used pixel and object classifiers, as the maximum-likelihood (ML) and nearest-neighbor (NN) algorithms [47,48], respectively, using the

same areas of interest. The pixel-based classifications were conducted using the ENVI software, and the object classifications using the eCognition software.

The ML method assumes that pixels of each class belong to a multivariate normal distribution and defines the probability density function for each class. Each pixel is assigned to the class that it has the highest probability of being in [49]. Comparatively, the NN classifier uses spatial features to classify the object, based on the closest training examples and on the class in which its neighbors have been classified. The NN classification required a previous segmentation step. This phase was performed using a multilevel segmentation approach, and in addition to the tri-bands orthoimage, the normalized difference vegetation index and digital surface models were used as input layers. The multiresolution segmentation algorithm was used to generate the image objects. Four levels of segmentation were applied, which defined the color and shape parameters, with the scale parameter increased at each level (Figure 4). The scale parameter was set to define the level of heterogeneity. Each level was evaluated by photo-interpretation. The optimized level was generated by combining the object levels. The optimized level comprised large segments in homogeneous areas and distinctively smaller image objects that represented small-scale structures and heterogeneous regions [50,51]. The class sample shapes were imported in the eCognition software to identify the objects that corresponded to the areas of interest. Therefore, the sample level was created by chess-board segmentation. Finally, the classification procedure was applied to image objects at the optimized level.

To create a comparable classification with pixel-based products, only the mean green, mean red, and mean NIR features were used.
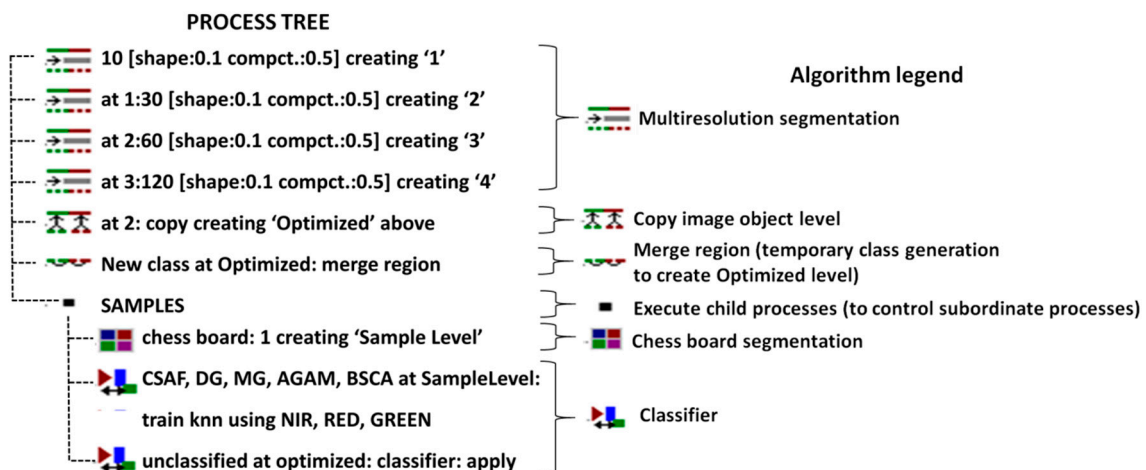
PROCESS TREE

10 [shape:0.1 compct.:0.5] creating '1'	**Algorithm legend**
at 1:30 [shape:0.1 compct.:0.5] creating '2'	Multiresolution segmentation
at 2:60 [shape:0.1 compct.:0.5] creating '3'	
at 3:120 [shape:0.1 compct.:0.5] creating '4'	
at 2: copy creating 'Optimized' above	Copy image object level
New class at Optimized: merge region	Merge region (temporary class generation to create Optimized level)
SAMPLES	Execute child processes (to control subordinate processes)
chess board: 1 creating 'Sample Level'	Chess board segmentation
CSAF, DG, MG, AGAM, BSCA at SampleLevel: train knn using NIR, RED, GREEN	Classifier
unclassified at optimized: classifier: apply	

Figure 4. The eCognition process tree used for the segmentation and object classification steps.

To improve the comparison quality, the support vector machine (SVM) algorithm was applied for both pixel-based and object-based classifiers. The SVM method seeks to determine the optimal separating hyperplane between classes by focusing on the training cases (vector support) that are placed at the edge of the class descriptors [52]. Training cases other than support vectors are discarded. In this way, fewer training samples are effectively used. Therefore, a high classification accuracy is achieved with small training sets [53]. The SVM used for classification has the advantages of solving sparse sampling and nonlinear and global optimum problems, compared to other classifiers for satellite imagery classification [54].

The implementation of SVM in the ENVI software based on the pairwise classification strategy is a multiclass classification method that combines all of the comparisons for each pair of classes [55]. The SVM pixel (SVMPi) classification output represents the decision values of each pixel for each class, which are used for the probability estimations. Among the available mathematical kernel functions, the linear function was applied. For the penalty parameter field (Harris Geospatial solution, ENVI 5.2), the value of 100 was used, which represents a parameter that controls the trade-off between

allowing training errors and forcing rigid margins. Based on the same theoretical approach, using the eCognition software, the equal function and parameters were applied at the optimized level to perform the corresponding object classification (SVMObj).

Once the classifications were performed, their accuracies were evaluated. The agreement between each classification and ground truth was assessed, as represented by 300 control points.

The pixel-by-pixel comparison provided the confusion matrix with dimensions equal to the number of classes, the overall accuracy, and the Kappa coefficient (*K*). For the object-based approach, the classification result was exported in a raster format to carry out the comparison. The *K* compares global accuracy with an expected global accuracy, taking into account random chance. *K* >0.80 represents strong agreement and *K* <0.40 represents poor agreement [56]. The user accuracy, producer accuracy, and *K-Conditional* were also calculated from a single confusion matrix. The first provides the probability that a random pixel extracted from among those belonging to class *i* in the reference belongs to class *i* in the classification. The producer accuracy, instead, defines whether a randomly chosen pixel among those belonging to class *j* in the classification also belongs to class *j* in the reference data [57]. As for *K*, *K-Conditional* represents the agreement between the reference pixels and those classified, as calculated for each class.

2.4. Statistical Classification Comparison

To determine the better performing classification method between pixel-based and object-based classification, three tests were carried out: TEST 1, TEST 2, and TEST 3.

TEST 1 established the significance of the difference in the accuracy between two maps with independent Kappa coefficients. Once establishing the null hypothesis, that the expected *K* values of the two statistics considered for each comparison (1 = first algorithm; 2 = second algorithm) were the same (i.e., no significant difference), the Student's *t* was applied [47,58], as in Equation (1):

$$z = \frac{K_1 - K_2}{\sqrt{\sigma_1^2 + \sigma_2^2}} \quad , \qquad z \sim N(0,1) \tag{1}$$

where σ_1^2 and σ_2^2 represent the estimated variances of the derived *K* coefficients.

To calculate the required variance values associated with the *K* and *K-Conditional* coefficients, a Fortran program was implemented using the σ formula proposed by Rossiter (2004) [59]. Considering that *z* follows a normal normalized distribution and the significance level $\alpha = 0.10$, with a consequently confidence limit of 1.65, the hypothesis was accepted for the test statistic *z* of |z| ≤1.65.

TEST 2 evaluated the significance of the difference between two independent proportions [60], using Equation (2), which takes into account the correction for continuity [58]:

$$z = \frac{\left| \frac{x_1}{n_1} - \frac{x_2}{n_2} \right| - \frac{1}{2}\left(\frac{1}{n_1} + \frac{1}{n_2} \right)}{\sqrt{p(1-p)\left(\frac{1}{n_1} + \frac{1}{n_2} \right)}}, \qquad z \sim N(0,1) \tag{2}$$

where x_1 and x_2 are the numbers of correctly allocated cases in two samples of size n_1 and n_2, respectively, and $p = (x_1 + x_2)/(n_1 + n_2)$. The statistical significance of the difference between two classification maps is verified through *z*, which follows a normal normalized distribution, in the same way as with the previous comparison of *K*.

TEST 3 was based on McNemar's test [60], which is suitable for comparisons of related samples. Equation (3) takes into account the correction for continuity [61]:

$$X_1^2 = \frac{\left(\left| f_{12} - f_{21} \right| - 1 \right)^2}{f_{12} + f_{21}} \tag{3}$$

This non-parametric test uses a confusion matrix, of 2×2 dimensions, in which f_{ij} indicates the frequency of sites lying in confusion element i, j, as reported in the example in Table 1.

Table 1. The matrix elements used in Equation (3) [61].

		Classification 2	
		Correct	Not Correct
Classification 1	Correct	f_{11}	f_{12}
	Not correct	f_{21}	f_{22}

The McNemar statistic follows a chi-squared distribution X_1^2 with one degree of freedom, and its square root follows a normal normalized distribution. Therefore, the statistical significance of the difference between the two classification maps is evaluated as with the previous tests.

The continuity correction that is considered in TEST 2 and TEST 3 is particularly important when the sample size used is small [62].

In the first step, these tests were applied for the same classification technique at both the global and single class levels. Then, the tests were applied to compare the statistical significance of the accuracy between the two algorithms that demonstrated smaller errors in previous comparisons.

3. Results

3.1. Classification Results

Both of the classification algorithms recognized the five vegetation classes considered as irregular belts almost parallel to the coastline: BSCA, AGAM, MG, GD, and CSAF (see Figure 2).

For the pixel-based classification (Figure 5), the single vegetation strips showed nonhomogeneous coverage because many of the pixels were assigned to classes that were different from those of the membership (Figure 5, subplots a and b). The pixel distributions of the MG, GD, AGAM, and CSAF classes (i.e., all except for the BSCA class) were characterized by a 'salt and pepper' effect that makes the definition of the class contours difficult. This effect is particularly evident in the ML map over several zones, such as for the northern area, which was strongly affected by both natural and anthropic effects (Figure 5, subplots a1 and b1). Indeed, while the SVMPi showed greater sandy coverage, in the ML results, the MG and DG pixels prevailed in these areas. As can be seen from Figure 5, both of these pixel approaches recognized the shape of the tree (*Populus × canadensis*) that was included in the CSAF class (Figure 5, subplots a1 and b1, center left), although its composition was confused for both of these methods. The *Populus × canadensis* tree composition was more appropriate and homogeneous in the SVMPi result compared to the ML map, where several pixels were wrongly tagged as GD. In general, many pixels that belonged to the CSAF strip were erroneously classified as GD. The details shown in Figure 5, subplots a2 and b2, indicate other relevant errors, such as: (1) several BCSA pixels along the footpaths were incorrectly associated with MG or GD cover; (2) some of the AMAG pixels were erroneously recognized in proximity to the CSAF class, where the morphological and environmental conditions are not suitable for this vegetal community; and (3) bare sand footpaths were recognized as covered by GD pixels. In general, the most confused classes were AMAG, MG, and GD, while the BCSA class was more homogeneous and more correctly discriminated from the rest of the scene. The aforementioned examples of confusion were more evident for the ML class. The main difference between these two pixel-base results is the number of pixels classified as MG and GD. The area covered by the MG class in the SVMPi map was greater than the MG zone of the ML map, with the inverse situation seen for the GD class (Table 2).
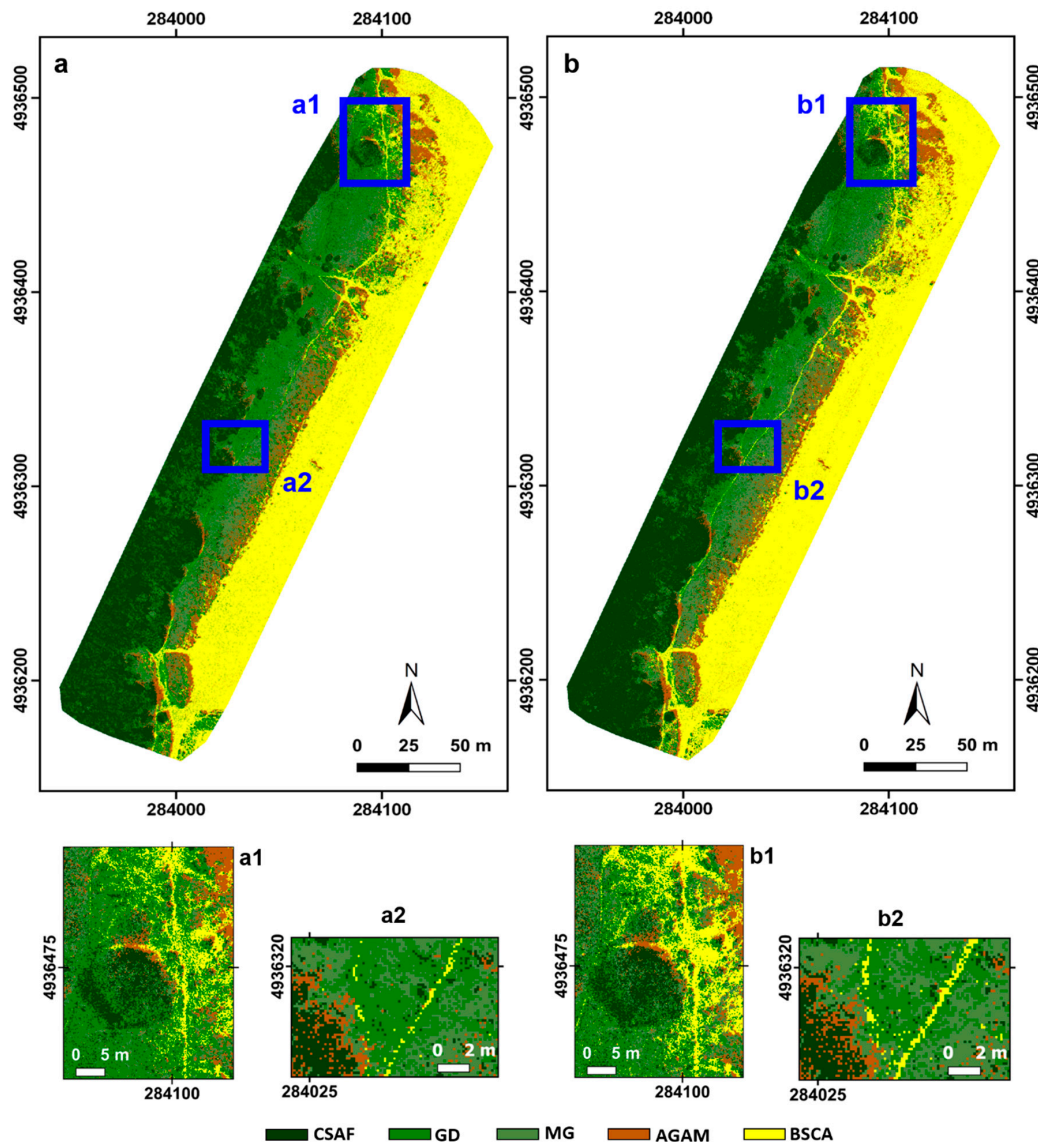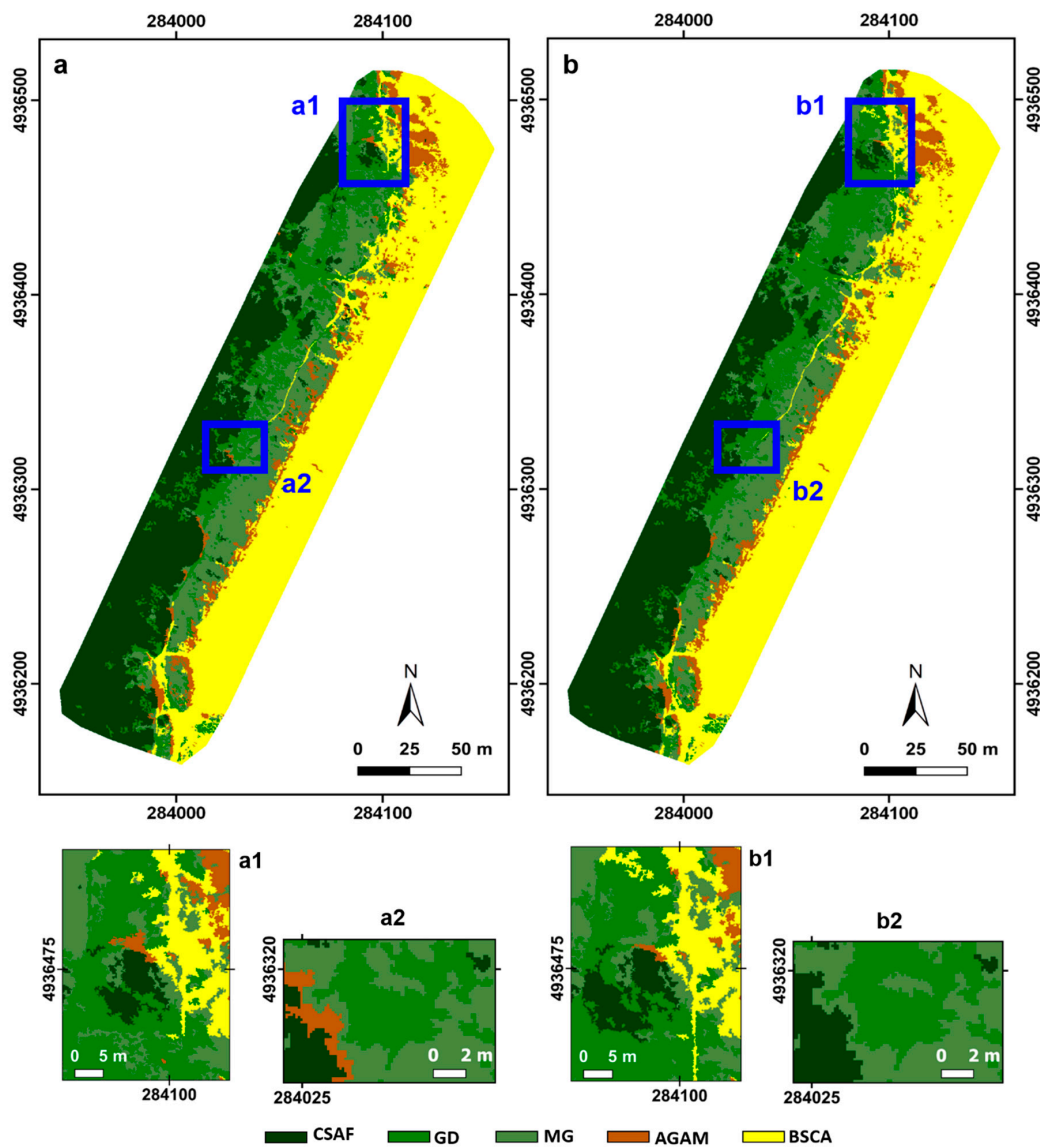
Figure 5. Pixel-based classification of the Casal Borsetti dune vegetation. (**a**) Maximum likelihood classification. (**b**) Support vector machine pixel classification. (**a1,b1**) 'Salt and pepper' effects and the *Populus × canadensis* tree. (**a2,b2**) Footpath classification.

For the application of the object-classification algorithms, the five vegetation classes were also identified (Figure 6, subplots a and b). The classes were more uniform than for the pixel-based results (Figure 5), and the confused zones were distributed along the perimeter of each class.

At the single-element level, the object maps showed less information. The tree located in the northern area (*Populus × canadensis*) was partially classified as CSAF, while several objects were associated with MG or GD (Figure 6, subplots a1 and b1). Moreover, it was only possible to identify this tree shape in the SVMObj map (Figure 6, subplot b1), because the NN classification (Figure 6, subplot a1) did not provide clear enough information. In addition, Figure 6, subplots a1 and b1, shows a greater presence of sand in the northern part of the dune compared to the pixel-based method (Figure 5, subplots a1 and b1).

Comparing Figure 5, subplots a2 and b2, with the details in Figure 6, subplots a2 and b2, another difference between the pixel and object methods can be seen for the sand footpaths. These were well-identified with the pixel-based method, while they were not recognized using the object-based approach.

Figure 6. Object-based classification of the Casal Borsetti dune vegetation. (**a**) Nearest neighbor classification. (**b**) Support vector machine object classification. (**a1,b1**) *Populus × canadensis* tree classification. (**a2,b2**) Missed footpath classification.

Table 2. Vegetation community cover and extension for each classification methodology. For abbreviations, see main text.

Vegetation Community	Classification Methodology							
	ML		SVMPi		NN		SVMObj	
	Cover (%)	Extension (m²)	Cover (%)	Extension (m²)	Cover (%)	Extension (m²)	Cover (%)	Extension (m²)
BSCA	34.4	9763	36.1	10,251	36.6	10,412	36.8	10,469
CSAF	25.9	7349	28.5	8082	26.6	7558	26.8	7617
MG	12.8	3647	16.3	4628	19.1	5433	16.8	4782
GD	19.0	5398	10.8	3082	12.3	3511	14.3	4073
AGAM	7.9	2241	8.3	2359	5.4	1546	5.3	1520
Total	100.0	28,398	100.0	28,402	100.0	28,460	100.0	28,460

All previous considerations were confirmed by the confusion matrices given in Table 3, which provides a quantitative reading of the classification results. The ML and SVMPi results showed a

lower global accuracy, with both <80%, while for the object classification, this was >80%. The global *K*s followed the same behavior as the global accuracies. In particular, considering the ML and SVMPi comparison and the NN and SVMObj comparison separately, the main diagonal values of the pixel classifications are almost always lower or equal to the corresponded values of the object classifications. For the ML map, the number of correct pixels is only higher than the NN classification for the GD class.

For the ML and SVMPi maps, the MG was the most confused class, with omission errors of 47.1% (24 missing pixels, of 51 true total pixels) and 43.1% (22/51 pixels missing), respectively (Tables 3 and 4). For the ML results, almost 42% of the MG omission error (10/24 pixels missing) is concentrated in the GD class (Table 3), while for the SVMPi map, the MG true pixels are distributed among the AGAM, GD, and CSAF covers (Table 3). Instead, the largest number of pixels associated with classes other than those of the reference is related to the GD class for ML, with a commission error of 46.1% (35 added pixels, of 76 total classified pixels; Table 4), and the MG class for SVMPi, with a commission error of 39.6% (19/48 pixels classified; Table 4). From Table 4, the producer accuracy was calculated. In the pixel-based algorithms, the class that was ranked most accurately was BSCA, with associated values of 86.5% for ML and 91.9% for SVMPi.

For the object-based classification results (Tables 3 and 4), the most confused class was GD in the NN map. For the 19 pixels not assigned (Table 4), 68.4% was classified as MG cover (Table 3), for the highest commission error (36.1%, i.e., 22/61 pixels classified; Table 4). Instead, for the SVMObj classification, the MG class showed the highest omission error (27.5%, i.e., 14/51 pixels missing), with almost 64.3% of these pixels classified as GD. The confusion between these classes was confirmed by the high commission error for GD (32.2%, i.e., 19/59 pixels classified; Table 4).

However, it should be emphasized that in the SVMObj results, the higher omission errors of the other classes did not differ much from the error related to MG. The BSCA producer accuracy achieved with the object-based techniques (93.2%), which was the same for NN and SVMObj, was the highest obtained among the several classes. However, some pieces of sand footpaths in the object-based classification maps were included in the GD or MG covers.

Table 3. Confusion matrices for each of the image classification methodologies. For abbreviations, see main text.

Classification Methodology	Vegetation Community	Ground Truth (pixels)						Overall Accuracy	*Kappa*
		BSCA	AGAM	GD	MG	CSAF	Total	(%)	
ML	BSCA	**64**	7	2	0	0	73		
	AGAM	1	**34**	1	7	2	45		
	GD	7	3	**41**	10	15	76	72.7	0.64
	MG	2	7	5	**27**	3	44		
	CSAF	0	1	5	7	**49**	62		
SVMPi	BSCA	**68**	4	3	1	0	76		
	AGAM	1	**40**	1	6	2	50		
	GD	3	1	**39**	7	10	60	76.3	0.70
	MG	2	6	7	**29**	4	48		
	CSAF	0	1	4	8	**53**	66		
NN	BSCA	**69**	6	3	1	0	79		
	AGAM	1	**39**	2	3	1	46		
	GD	3	1	**35**	6	6	51	80.3	0.75
	MG	1	5	13	**39**	3	61		
	CSAF	0	1	1	2	**59**	63		
SVMObj	BSCA	**69**	7	3	1	0	80		
	AGAM	2	**41**	3	2	1	49		
	GD	3	1	**40**	9	6	59	82.0	0.77
	MG	0	3	7	**37**	3	50		
	CSAF	0	0	1	2	**59**	62		
	Total	74	52	54	51	69	300		

Table 4. Commission and omission errors for each of the vegetation communities. For abbreviations, see main text.

Vegetation Community	Errors (pixels)							
	ML		SVMPi		NN		SVMObj	
	Commission	Omission	Commission	Omission	Commission	Omission	Commission	Omission
BSCA	9/73	10/74	8/76	6/74	10/79	5/74	11/80	5/74
AGAM	11/45	18/52	10/50	12/52	7/46	13/52	8/49	11/52
GD	35/76	13/54	21/60	15/54	16/51	19/54	19/59	14/54
MG	17/44	24/51	19/48	22/51	22/61	12/51	13/50	14/51
CSAF	13/62	20/69	13/66	16/69	4/63	10/69	3/62	10/69

3.2. Classification Results Comparison

The outcomes of TEST 1 applied to the pixel-based classification reveal that the differences in accuracy between the two pixel-based maps at both the global and single class level are not significant (Table 5). In addition, TEST 2 confirms that the ML and SVMPi classifications are statistically similar (Table 5).

For TEST 3, based on four combinations of correct and incorrect pixel frequencies in both of the maps considered, the classifications are globally different (z = 2.65 > 1.65). This is particularly due to the AGAM community, as the only class that does not pass the test. The analysis of the frequencies used for TEST 3 reveals that the ML method is the least accurate method for the AGAM class. Indeed, the calculations of TEST 3 show that almost 12% of the 52 ground truth pixels were classified incorrectly only for ML, while the same pixels were correct for SVMPi; vice versa, there are no pixels that were not correctly classified only for SVMPi. For the AGAM class, the lower accuracy for ML is also confirmed by the higher commission and omission errors compared with the corresponding SVMPi errors (Table 4).

As for the pixel-based classification, as for the object-based classification, the outcomes of TEST 1 show that the differences in the accuracy between the two object-based classification maps at both the global and single class level are not significant (Table 6). The TEST 2 results confirm that the NN and SVMObj classifications are similar (Table 6). Additionally, for TEST 3, these classifications are not different, except for the GD cover, at both the global and individual class levels. The frequency analysis reveals that the NN method is the least accurate method; indeed, almost 8% of the 54 GD ground truth pixels were incorrectly classified for NN, while the same pixels were correctly classified for SVMObj; vice versa, there were no pixels incorrectly classified only for SVMObj. For the GD class, the lower accuracy of NN is also confirmed by the higher omission errors compared with the corresponding SVMObj errors (Table 4). Indeed, in both object-based maps, the highest number of error classifications is between the GD and MG classes. However, the MG cover classifications are not statistically different.

From the previous comparisons, it emerges that the most accurate methods are SVMPi and SVMObj. Therefore, a new statistical comparison of these two methods was performed to define the most appropriate for this dune vegetation classification. The findings of TEST 1 show that the accuracy difference between these two maps is not significant at both the global and single class level (Table 7). The TEST 2 results confirm that the SVMPi and SVMObj classifications are similar (Table 7). Instead, for the findings of TEST 3, the two classifications are globally different (z = 2.16 > 1.65). At the single class level, all of the classes pass the test, except for the MG cover, with a z value the same as the confidence limit (1.65). The analysis of the frequencies reveals that almost 26% of the 51 MG ground truth pixels were classified incorrectly for SVMPi, while they were correct for SVMObj; vice versa, only 10% were correctly classified for SVMPi and not for SVMObj (Table 7).

Table 5. Test results for the pixel-based classification, as a comparison of ML and SVMPi. For abbreviations, see main text.

Vegetation Community	TEST1			TEST2	TEST3	Confidence
	K-ML	K-SVMPi	z (K)	z (Propor.)	z (McNemar)	Limit (α=0.10)
BSCA	0.82	0.89	−1.07	0.79	1.50	
AGAM	0.59	0.72	−1.32	1.08	2.04	
GD	0.68	0.65	0.24	0.22	0.50	**1.65**
MG	0.45	0.49	−0.35	0.20	0.50	
CSAF	0.63	0.70	−0.77	0.58	1.22	
Global	**0.64**	**0.70**	**−1.19**	**1.21**	**2.65**	

Table 6. Test results for the object-based classification, as a comparison of NN and SVMObj. For abbreviations, see main text.

Vegetation Community	TEST1			TEST2	TEST3	Confidence
	K-NN	K-SVMObj	z (K)	z (Propor.)	z (McNemar)	Limit (α=0.10)
BSCA	0.91	0.91	0.01	−0.33	0.00	
AGAM	0.70	0.75	−0.45	0.23	0.71	
GD	0.58	0.68	−0.10	0.84	1.79	**1.65**
MG	0.71	0.68	0.34	0.23	0.50	
CSAF	0.82	0.82	−0.01	−0.24	0.71	
Global	**0.75**	**0.77**	**−0.42**	**0.42**	**1.11**	

Table 7. Test results of the comparison of the SVMPi and SVMObj classifications. For abbreviations, see main text.

Vegetation Community	TEST1			TEST2	TEST3	Confidence
	K-SVMPi	K-SVMObj	z (K)	z (Propor.)	z (McNemar)	Limit (α=0.10)
BSCA	0.89	0.91	−0.29	0.00	0.00	
AGAM	0.72	0.75	−0.26	0.00	0.00	
GD	0.65	0.68	−0.24	1.39	0.00	**1.65**
MG	0.49	0.68	−1.77	0.00	1.65	
CSAF	0.70	0.82	−1.43	1.09	1.44	
Global	**0.70**	**0.77**	**−1.45**	**1.61**	**2.16**	

4. Discussion

Before discussing the results, some considerations regarding the particularity of the site and the instruments involved in the data acquisition need to be addressed. As described above for the study area description, the selected site is included in the Po Delta Regional Park, and there are restrictions regarding access, authorized activities, and management of the dunes. Despite this, during the summer, tourism results in the establishment of a lot of footpaths, which destroys the vegetation communities and fosters wind erosion of the dunes [3,31,37]. Therefore, the local vegetation communities are often fragmented and interspersed with each other, which provides an atypical vegetation composition in the area. Although each plant species provides its own spectral signature based on the growth period, geographic location, climatic conditions, and level of disturbance [63,64], working at the vegetation community level reduces the species diversification and provides more solid results [65,66]. In addition to this, the contemporary ground truth botanical survey allowed a reliable dataset of 'known' pixels to be established to validate the vegetation maps. In particular, the extreme dynamic environment represented by this dune system, its cycling, exposure to sea storms, erosion, salty winds, and floating groundwater from one side require an accurate selection of the aerial acquisition period, and from the other side, the achieved vegetation community distribution can be considered descriptive for a relatively medium-to-long period of time [17,67].

For the equipment used, the three standard bands available with the multispectral camera (i.e., green, red, NIR) are considered necessary and sufficient to recognize the vegetation [68], but not to discriminate between and examine in-depth the characteristics of the single species [69]. Furthermore, this camera has the following technical limitations: an overlay of portions of the bandwidth, a large bandwidth with a low-slope front of the filter, and the inability to discriminate between uninteresting portions of the bands [40].

For the classification results, all of the four algorithms recognized the five classes of vegetation considered. Despite this, the maps that were derived from the pixel-based methods showed that class boundaries are not well defined due to the 'salt and pepper' effect that was spread throughout the extension of the dunes. This effect was especially evident in the ML map, as well as in the portion of dunes where a combination of the wind and recurring anthropic passage has reduced the vegetation growth. Indeed, for the ML map, these areas were mostly covered by the MG and DG pixels, while the SVMPi classification revealed the wider sandy cover, thus better identifying the actual field conditions (Figure 5, subplots a1, b1). This result is explained by the relationship between the pixel size (15 cm) and the different plant components acquired [40]. Indeed, a pixel size of 15 cm can include more plant elements (e.g., leaves, flowers, small branches, shadows), or it can be homogeneously occupied by a single element. Therefore, its spectral signature might represent a medium signature or might not include the other components of the same class [11]. Furthermore, considering that the same type of object can be contained in many classes (e.g., sand, grass), some pixels might be classified differently compared to the surrounding pixels [70].

The object-based classification was less exposed to these problems compared to the pixel-based approach. The presence of some pixels with different vegetation covers has no influence on the correct class assignment [46,54]. As confirmation of this, the more extended BSCA class in the northern section of the study area is coherent with the actual situation, and reflects the higher anthropic disturbance due to the sand mobilization in the close-by bathing establishment.

If, on one hand, the object-based classification provides vegetation class uniformity, on the other hand, it does not allow the identification of some single elements that were identified with the pixel-based approach. For example, the *Populus × canadensis* tree shape was well-defined in the pixel-based approach, while it was not recognizable in the object-based approach. In the same way, some objects classified as CSAF appeared in their correct location, but the shape reconstruction was lost. Other missing information with the object-based approach was the identification of the sand footpaths, which were almost totally incorporated into the surrounding vegetated classes.

The confusion matrix analysis of the four classification methods confirms the greater accuracy of the object-based approaches (Table 3), due to the clearer class definition obtained. At the opposite end of the spectrum, the 'salt and pepper' effects reduce the accuracy of pixel-based methods [70].

Considering the pixel-based elaboration, the ML method shows a more coarse accuracy compared to SVMPi, as indirectly confirmed by the global TEST 3 result (Table 5). The AGAM class was differently recognized among the two pixel-based algorithms, but the most difficult class to identify was MG, due to its wide and complex presence in the dune vegetation structure. The MG and GD classes were often confused because of the de-structuring of the GD vegetation that was caused by the anthropogenic disturbance, which generates short biological growing cycles that are typical of the MG class. This problem is also seen for the object-based classification, but with an impact of only 14% on the mean class errors (Table 4). The errors of commissions and omissions with SVMPi were generally lower than those for ML (Table 4). In particular, a greater producer accuracy of the BCSA class was seen, especially along the footpaths, which appeared more defined and lengthened.

The differences in the classification between the NN and SVMObj methods are not significant, except for the GD class. However, the SVM algorithm was more accurate, and it should be the most reliable method to be applied to dune monitoring, especially in the case of characteristics similar to those of Casal Borsetti. The same conclusion was reported by Wang et al. [71] in a study where they

compared pixel-based and object-based approaches in mangrove classification, as well as by Zhai et al. for a rubber plantation [72].

The choice between the SVM pixel-based and the SVM object-based techniques also depends on the level of detail required. According to TEST 3 (Table 7), at the global level, the results of these two techniques were different only because of the classification of the MG cover. However, this class is an opportunistic vegetation community that grows where disturbance is higher. Indeed, the z obtained for MG was the same as the threshold imposed for not passing the test (i.e., z = 1.65). Therefore, even if the SVMObj shows the best accuracy, as reported by Gao et al. [54], considering the accuracies of these two methods as similar does not induce significant errors, as already demonstrated through TEST 1 and TEST 2 (Table 7).

Based on the results of this study, a UAV equipped with a multispectral camera can be used for multi-year dune monitoring to provide a multitemporal classification of dune vegetation [73]. Moreover, based on the well-known relationships between dune vegetation communities and coastline status [74,75], both the equipment and methodology presented in this study can also be applied to future continuous monitoring of the coastline, in order to gather information on the coastal evolutionary status [76].

The authors should discuss the results and how they can be interpreted from the perspective of previous studies and the working hypotheses. The findings and their implications should be discussed in the broadest context possible. Future research directions may also be highlighted.

5. Conclusions

The aims of this study were to determine the applicability of multispectral data collected by a UAV platform for the identification/discrimination of fragmented and interspersed coastal dune vegetation communities, and to compare the pixel-based and object-based approaches to determine the better performing classification method.

The data acquired by the sensors installed on the UAV and elaborated with the SVM algorithm allowed the elaboration of reliable dune vegetation community maps with a high spatial resolution (0.15 m) and a global accuracy >80%. This system is cheaper and faster when compared to the traditional field surveys that are performed by botanical experts.

From the comparisons of the classification methods here, as NN, ML, SVMPi, and SVMObj, the SVM was the most accurate algorithm based on the statistical test results. From the numerical point of view, the SVMObj was the best performing approach. However, it has the disadvantage of including small elements (<1 m in size), such as single trees or footpaths, in the larger bordering classes, which impedes their suitable classification. In the case of limited extension, where the presence and variations of a single element can widely influence the final results, this aspect is a relevant limitation. For example, for the Casal Borsetti dune area, the protection of the relevant coastal habitat of the dune vegetation communities needs to be pursued by limiting the continuous human crossing. Therefore, the footpaths need to be clearly identified using the proposed methodology. Considering that the differences between SVMPi and SVMObj are not statistically significant, except for the MG class, the pixel technique is the most suitable for investigations that require greater levels of detail. The MG and GD classes are the most difficult to discriminate with a camera that only acquires the green, red, and infrared bands, as is the case for the camera used in this study. The entry onto the market of multi-spectral cameras with eight mono-band sensors (from visible to infrared) might also facilitate the more accurate identification of vegetation communities using a UAV.

Although the results obtained cannot be immediately generalized because they refer to a specific study site (i.e., Casal Borsetti dunes, Ravenna, Italy) that shows strong human disturbance and fragmented and interspersed dune vegetation communities, both the equipment used here and the classification approach appear portable, and can thus be applied to other dune sites.

Moreover, in light of the elevated spatial resolution of the vegetation maps produced, the authors believe that this system, the UAV data acquisition, and the SVM image classification approach, are

sufficiently sensitive to allow multitemporal and continuous monitoring of dune evolution in the near future, in terms of erosion and progradation-dominant phenomena. Ongoing studies are collecting data for the monitoring of coastal erosive/progradation dynamics through dune vegetation communities.

Author Contributions: Conceptualization of the study, M.D.G., N.G., and N.M.; methodology, M.D.G., M.D., F.G., and M.B.; software, M.D.G., M.D., F.G., and M.B.; validation, M.B.; investigation, N.M., N.G., and M.D.G.; data curation, M.D.G., M.B., N.M., M.D., and F.G.; writing—original draft, M.D.G. and N.G.; writing—review and editing, M.D.G. and N.G.; supervision, M.B. and M.D.

References

1. Gómez-Pina, G.; Muñoz-Perez, J.J.; Ramirez, J.L.; Ley, C. Sand dune management problems and techniques, Spain. *J. Coast. Res.* **2002**, *36*, 325–332. [CrossRef]

2. Drius, M.; Malavasi, M.; Acosta, A.T.R.; Ricotta, C.; Carranza, M.L. Boundary-based analysis for the assessment of coastal dune landscape integrity over time. *Appl. Geogr.* **2013**, *45*, 41–48. [CrossRef]

3. Sytnik, O.; Stecchi, F. Disappearing coastal dunes: Tourism development and future challenges, a case-study from Ravenna, Italy. *J. Coast. Conserv.* **2015**, *19*, 715–727. [CrossRef]

4. Malavasi, M.; Santoro, R.; Cutini, M.; Acosta, A.T.R.; Carranza, M.L. The impact of human pressure on landscape patterns and plant species richness in Mediterranean coastal dunes. *Plant Biosyst.* **2016**, *150*, 73–82. [CrossRef]

5. Janssen, J.A.M.; Rodwell, J.S.; Criado, M.G.; Arts, G.H.P.; Bijlsma, R.J.; Schaminee, J.H.J. European Red List of Habitats: Part 2. Terrestrial and Freshwater Habitats. European Union. 2016. Available online: https://publications.europa.eu/en/publication-detail/-/publication/22542b64-c501-11e7-9b01-01aa75ed71a1/language-en (accessed on 10 April 2019).

6. Sytnik, O.; Del Río, L.; Greggio, N.; Bonetti, J. Historical shoreline trend analysis and drivers of coastal change along the Ravenna coast, NE Adriatic. *Environ. Earth Sci.* **2018**, *77*, 779. [CrossRef]

7. Provoost, S.; Jones, M.L.M.; Edmondson, S.E. Changes in landscape and vegetation of coastal dunes in northwest Europe: A review. *J. Coast. Conserv.* **2011**, *15*, 207–226. [CrossRef]

8. Sciandrello, S.; Tomaselli, G.; Minissale, P. The role of natural vegetation in the analysis of the spatio-temporal changes of coastal dune system: A case study in Sicily. *J. Coast. Conserv.* **2015**, *19*, 199–212. [CrossRef]

9. Masselink, G.; Pattiaratchi, C.B. Seasonal changes in beach morphology along the sheltered coastline of Perth, Western Australia. *Mar. Geol.* **2001**, *172*, 243–263. [CrossRef]

10. Anthony, E.J.; Vanhée, S.; Ruz, M.-H. Short-term beach–dune sand budgets on the north sea coast of France: Sand supply from shoreface to dunes, and the role of wind and fetch. *Geomorphology* **2006**, *81*, 316–329. [CrossRef]

11. Hantson, W.; Kooistra, L.; Slim, P.A. Mapping invasive woody species in coastal dunes in the Netherlands: A remote sensing approach using LIDAR and high-resolution aerial photographs. *Appl. Veg. Sci.* **2012**, *15*, 536–547. [CrossRef]

12. Levin, N.; Levental, S.; Morag, H. The effect of wildfires on vegetation cover and dune activity in Australia's desert dunes: A multisensor analysis. *Int. J. Wildl. Fire* **2012**, *21*, 459–475. [CrossRef]

13. Fabbri, S.; Giambastiani, B.M.; Sistilli, F.; Scarelli, F.; Gabbianelli, G. Geomorphological analysis and classification of foredune ridges based on Terrestrial Laser Scanning (TLS) technology. *Geomorphology* **2017**, *295*, 436–451. [CrossRef]

14. Tsoar, H. Sand dunes mobility and stability in relation to climate. *Phys. A Stat. Mech. Appl.* **2005**, *357*, 50–56. [CrossRef]

15. Miller, T.E.; Gornish, E.S.; Buckley, H.L. Climate and coastal dune vegetation: Disturbance, recovery, and succession. *Plant Ecol.* **2009**, *206*, 97–104. [CrossRef]

16. Duran, O.; Silva, M.; Bezerra, L.; Herrmann, H.; Maia, L. Measurements and numerical simulations of the degree of activity and vegetation cover on parabolic dunes in north-eastern Brazil. *Geomorphology* **2008**, *102*, 460–471. [CrossRef]

17. Durán, O.; Moore, L.J. Vegetation controls on the maximum size of coastal dunes. *Proc. Natl. Acad. Sci. USA* **2013**, *110*, 17217–17222. [CrossRef]

18. Mathew, S.; Davidson-Arnott, R.G.D.; Ollerhead, J. Evolution of a beach–dune system following a catastrophic storm overwash event: Greenwich Dunes, Prince Edward Island, 1936–2005. *Can. J. Earth Sci.* **2010**, *47*, 273–290. [CrossRef]

19. Schmidt, K.; Skidmore, A. Spectral discrimination of vegetation types in a coastal wetland. *Remote Sens. Environ.* **2003**, *85*, 92–108. [CrossRef]

20. Acosta, A.; Carranza, M.L.; Izzi, C.F. Combining land cover mapping of coastal dunes with vegetation analysis. *Appl. Veg. Sci.* **2009**, *8*, 133–138. [CrossRef]

21. Ajedegba, J.O.; Perotto-Baldivieso, H.L.; Jones, K.D. Coastal Dune Vegetation Resilience at South Padre Island, Texas: A Spatiotemporal Evaluation of the Landscape Structure. *J. Coast. Res.* **2019**, *35*, 534–544. [CrossRef]

22. Saye, S.; Van Der Wal, D.; Pye, K.; Blott, S.; Blott, S. Beach–dune morphological relationships and erosion/accretion: An investigation at five sites in England and Wales using LIDAR data. *Geomorphology* **2005**, *72*, 128–155. [CrossRef]

23. Brock, J.C.; Purkis, S.J. The Emerging Role of Lidar Remote Sensing in Coastal Research and Resource Management. *J. Coast. Res.* **2009**, *53*, 1–5. [CrossRef]

24. Mancini, F.; Dubbini, M.; Gattelli, M.; Stecchi, F.; Fabbri, S.; Gabbianelli, G. Using Unmanned Aerial Vehicles (UAV) for High-Resolution Reconstruction of Topography: The Structure from Motion Approach on Coastal Environments. *Remote Sens.* **2013**, *5*, 6880–6898. [CrossRef]

25. Suanez, S.; Cariolet, J.-M.; Fichaut, B. Monitoring of recent morphological changes of the dune of Vougot beach (Brittany, France) using differential GPS. *Shore Beach* **2010**, *78*, 37–47.

26. Casella, E.; Rovere, A.; Pedroncini, A.; Stark, C.P.; Casella, M.; Ferrari, M.; Firpo, M. Drones as tools for monitoring beach topography changes in the Ligurian Sea (NW Mediterranean). *Geo-Mar. Lett.* **2016**, *36*, 151–163. [CrossRef]

27. Anderson, K.; Gaston, K.J. Lightweight unmanned aerial vehicles will revolutionize spatial ecology. *Front. Ecol. Environ.* **2013**, *11*, 138–146. [CrossRef]

28. Guillot, B.; Pouget, F. UAV application in coastal environment, example of the Oleron island for dunes and dikes survey. *ISPRS Int. Arch. Photogramm. Remote Sens. Spat. Inf. Sci.* **2015**, *3*, 321–326. [CrossRef]

29. Gonçalves, J.; Henriques, R. UAV photogrammetry for topographic monitoring of coastal areas. *ISPRS J. Photogramm. Remote Sens.* **2015**, *104*, 101–111. [CrossRef]

30. Airoldi, L.; Ponti, M.; Abbiati, M. Conservation challenges in human dominated seascapes: The harbour and coast of Ravenna. *Reg. Stud. Mar. Sci.* **2016**, *8*, 308–318. [CrossRef]

31. Semeoshenkova, V.; Newton, A.; Contin, A.; Greggio, N. Development and application of an Integrated Beach Quality Index (BQI). *Ocean Coast. Manag.* **2017**, *143*, 74–86. [CrossRef]

32. Corbau, C.; Simeoni, U.; Melchiorre, M.; Rodella, I.; Utizi, K. Regional variability of coastal dunes observed along the Emilia-Romagna littoral, Italy. *Aeolian Res.* **2015**, *18*, 169–183. [CrossRef]

33. Piccoli, F.; Merloni, N.; Corticelli, S. *Carta della Vegetazione 1:25.000 della Stazione Pineta di San Vitale e Pialasse di Ravenna (Parco Regionale del Delta del Po)*; Regione Emilia-Romagna: Bologna, Italy, 1999.

34. Merloni, N.; Piccoli, F. Comunità vegetali rare e minacciate delle stazioni ravennati del Parco del Delta del Po (Regione Emilia-Romagna). *Fitosociologia* **2007**, *44*, 67–76.

35. Sburlino, G.; Buffa, G.; Filesi, L.; Gamper, U.; Ghirelli, L. Phytocoenotic diversity of the N-Adriatic coastal sand dunes—The herbaceous communities of the fixed dunes and the vegetation of the interdunal wetlands. *Plant Sociol.* **2013**, *50*, 57–77.

36. Valentini, E.; Taramelli, A.; Filipponi, F.; Giulio, S. An effective procedure for EUNIS and Natura 2000 habitat type mapping in estuarine ecosystems integrating ecological knowledge and remote sensing analysis. *Ocean Coast. Manag.* **2015**, *108*, 52–64. [CrossRef]

37. Merloni, N.; Rigoni, P.; Zanni, F. La vegetazione delle dune litoranee nella Riserva Naturale di Foce Bevano. In *Spiagge e dune dell'Alto Adriatico*; Corpo Forestale dello Stato: La Greca Arti Grafiche, Forlì, Italy, 2015.

38. Lazzari, G.; Merloni, N.; Saiani, D. Flora delle Riserve Naturali dello Stato nell'area costiera di Ravenna Parco Delta del Po-Emilia Romagna. *Quad. dell'Ibis* **2009**, *3*, 48.
39. TETRACAM Inc. *ADC Micro Camera User's Guide*; Tetracam Inc.: Chatsworth, CA, USA, 2013.
40. Candiago, S.; Remondino, F.; De Giglio, M.; Dubbini, M.; Gattelli, M. Evaluating Multispectral Images and Vegetation Indices for Precision Farming Applications from UAV Images. *Remote Sens.* **2015**, *7*, 4026–4047. [CrossRef]
41. Ullman, S. The interpretation of structure from motion. *Proc. R. Soc. Lond. Ser. B Biol. Sci.* **1979**, *203*, 405–426.
42. Sanz-Ablanedo, E.; Chandler, J.H.; Rodríguez-Pérez, J.R.; Ordóñez, C. Accuracy of Unmanned Aerial Vehicle (UAV) and SfM Photogrammetry Survey as a Function of the Number and Location of Ground Control Points Used. *Remote Sens.* **2018**, *10*, 1606. [CrossRef]
43. De Giglio, M.; Goffo, F.; Greggio, N.; Merloni, N.; Dubbini, M.; Barbarella, M. Satellite and unmanned aerial vehicle data for the classification of sand dune vegetation. *ISPRS Int. Arch. Photogramm. Remote Sens. Spat. Inf. Sci.* **2017**, *42*, 43–50. [CrossRef]
44. Castagneti, C.; Casula, G.; Dubbini, M.; Capra, A. Adjustment and transformation strategies of ItalPoSPermanent GNSS Network. *Ann. Geophys.* **2009**, *52*. Available online: http://hdl.handle.net/2122/5204 (accessed on 13 June 2019).
45. Leica Geosystem "White Paper: GPS Spider-NET—Take It to the MAX". Available online: https://www.smartnetna.com/documents/Leica_GPS_SpiderNET-Take_it_to_the_MAX_June2005_en.pdf (accessed on 14 April 2019).
46. Liu, D.; Xia, F. Assessing object-based classification: Advantages and limitations. *Remote Sens. Lett.* **2010**, *1*, 187–194. [CrossRef]
47. Gao, Y.; Mas, J.F. A Comparison of the Performance of Pixel-Based and Object-Based Classifications Over Images With Various Spatial Resolutions. *Online J. Earth Sci.* **2008**, *2*, 27–35.
48. Whiteside, T.G.; Boggs, G.S.; Maier, S.W. Comparing object-based and pixel-based classifications for mapping savannas. *Int. J. Appl. Earth Obs. Geoinf.* **2011**, *13*, 884–893. [CrossRef]
49. Lillesand, T.; Kiefer, R.W.; Chipman, J. *Remote Sensing and Image Interpretation*; John Wiley & Sons: New York, NY, USA, 2014.
50. Franci, F.; Spreafico, M. Processing of remote sensing data for the estimation of rock block size distribution in landslide deposits. In *Landslides and Engineered Slopes. Experience, Theory and Practice*; CRC Press: Boca Raton, FL, USA, 2016.
51. Taubenböck, H.; Esch, T.; Wurm, M.; Roth, A.; Dech, S. Object-based feature extraction using high spatial resolution satellite data of urban areas. *J. Spat. Sci.* **2010**, *55*, 117–132. [CrossRef]
52. Tzotsos, A.; Argialas, D. Support Vector Machine Classification for Object-Based Image Analysis. In *Object-Based Image Analysis*; Springer: New York, NY, USA, 2008; pp. 663–677.
53. Mercier, G.; Lennon, M. Support vector machines for hyperspectral image classification with spectral-based kernels. In Proceedings of the 2003 IEEE International Geoscience and Remote Sensing Symposium, IGARSS'03, Toulouse, France, 21–25 July 2003; Volume 1, pp. 288–290.
54. Gao, Z.; Liu, X. Support vector machine and object-oriented classification for urban impervious surface extraction from satellite imagery. In Proceedings of the 2014 Third International Conference on Agro-Geoinformatics, Beijing, China, 11–14 August 2014.
55. Wu, T.-F.; Lin, C.-J.; Weng, R.C. Probability Estimates for Multi-class Classification by Pairwise Coupling. *J. Mach. Learn. Res.* **2004**, *5*, 975–1005. [CrossRef]
56. Landis, J.R.; Koch, G.G. The measurement of observer agreement for categorical data. *Biometrics* **1977**, *33*, 159–174. [CrossRef]
57. Story, M.; Congalton, R.G. Accuracy assessment: A users perspective. *Photogramm. Eng. Remote Sens.* **1986**, *52*, 397–399.
58. Barbarella, M.; De Giglio, M.; Panciroli, L.; Greggio, N. Satellite data analysis for identification of groundwater salinization effects on coastal forest for monitoring purposes. *Proc. Int. Assoc. Hydrol. Sci.* **2015**, *368*, 325–330. [CrossRef]
59. Rossiter, D.G. *Statistical Methods for Accuracy Assessment of Classified Thematic Maps*; Technical Note; International Institute for Geo-Information Science and Earth: Enschede, The Netherlands, 2004.
60. Foody, G.M. Thematic map comparison. *Photogramm. Eng. Remote Sens.* **2004**, *70*, 627–633. [CrossRef]
61. Fleiss, J. *Statiscal Methods for Rates and Proportions*, 2nd ed.; Wiley: New York, NY, USA, 1981.

62. Neter, J.; Wasserman, W.; Whitmore, G.A. *Applied Statistics*; Allyn and Bacon: Boston, MA, USA, 1993.
63. Carter, G.A.; Knapp, A.K. Leaf optical properties in higher plants: Linking spectral characteristics to stress and chlorophyll concentration. *Am. J. Bot.* **2001**, *88*, 677–684. [CrossRef]
64. Walsh, S.J.; McCleary, A.L.; Mena, C.F.; Shao, Y.; Tuttle, J.P.; Gonzalez, A.; Atkinson, R. QuickBird and Hyperion data analysis of an invasive plant species in the Galapagos Islands of Ecuador: Implications for control and land use management. *Remote Sens. Environ.* **2008**, *112*, 1927–1941. [CrossRef]
65. Jiménez, M.; Díaz-Delgado, R. Towards a standard plant species spectral library protocol for vegetation mapping: A Case Study in the Shrubland of Doñana National Park. *ISPRS Int. J. Geo-Inf.* **2015**, *4*, 2472–2495. [CrossRef]
66. Hernandez-Santin, L.; Rudge, M.L.; Bartolo, R.E.; Erskine, P.D. Identifying Species and Monitoring Understorey from UAV-Derived Data: A Literature Review and Future Directions. *Drones* **2019**, *3*, 9. [CrossRef]
67. Jacobberger, P.A. Reflectance characteristics and surface processes in stabilized dune environments. *Remote Sens. Environ.* **1989**, *28*, 287–295. [CrossRef]
68. Peñuelas, J.; Filella, L. Technical focus: Visible and near-infrared reflectance techniques for diagnosing plant physiological status. *Trends Plant Sci.* **1998**, *3*, 151–156. [CrossRef]
69. Immitzer, M.; Vuolo, F.; Atzberger, C. First Experience with Sentinel-2 Data for Crop and Tree Species Classifications in Central Europe. *Remote Sens.* **2016**, *8*, 166. [CrossRef]
70. Yu, Q.; Gong, P.; Clinton, N.; Biging, G.; Kelly, M.; Schirokauer, D. Object-based Detailed Vegetation Classification with Airborne High Spatial Resolution Remote Sensing Imagery. *Photogramm. Eng. Remote Sens.* **2006**, *72*, 799–811. [CrossRef]
71. Wang, L.; Sousa, W.P.; Gong, P. Integration of object-based and pixel-based classification for mapping mangroves with IKONOS imagery. *Int. J. Remote Sens.* **2004**, *25*, 5655–5668. [CrossRef]
72. Zhai, D.; Dong, J.; Cadisch, G.; Wang, M.; Kou, W.; Xu, J.; Xiao, X.; Abbas, S. Comparison of pixel- and object-based approaches in phenology-based rubber plantation mapping in fragmented landscapes. *Remote Sens.* **2018**, *10*, 44. [CrossRef]
73. Van Iersel, W.; Straatsma, M.; Middelkoop, H.; Addink, E. Multitemporal Classification of River Floodplain Vegetation Using Time Series of UAV Images. *Remote Sens.* **2018**, *10*, 1144. [CrossRef]
74. Bitton, M.C.A.; Hesp, P.A. Vegetation dynamics on eroding to accreting beach-foredune systems, Florida panhandle. *Earth Surf. Process. Landf.* **2013**, *38*, 1472–1480. [CrossRef]
75. Feagin, R.A.; Figlus, J.; Zinnert, J.C.; Sigren, J.; Martínez, M.L.; Silva, R.; Smith, W.K.; Cox, D.; Young, D.R.; Carter, G. Going with the flow or against the grain? The promise of vegetation for protecting beaches, dunes, and barrier islands from erosion. *Front. Ecol. Environ.* **2015**, *13*, 203–210. [CrossRef]
76. Konlechner, T.M.; Kennedy, D.M.; Cousens, R.D.; Woods, J.L.D. Patterns of early-colonising species on eroding to prograding coasts; implications for foredune plant communities on retreating coastlines. *Geomorphology* **2019**, *327*, 404–416. [CrossRef]